INTERFACE

rsif.royalsocietypublishing.org

Research

Cite this article: Tournus M, Kirshtein A, Berlyand LV, Aranson IS. 2015 Flexibility of bacterial flagella in external shear results in complex swimming trajectories. *J. R. Soc. Interface* **12**: 20140904.
http://dx.doi.org/10.1098/rsif.2014.0904

Received: 13 August 2014
Accepted: 13 October 2014

Subject Areas:
mathematical physics, biophysics

Keywords:
elasticity, flagellum, non-periodic trajectories, microswimmer

Author for correspondence:
M. Tournus
e-mail: tournus.magali@gmail.com

Electronic supplementary material is available at http://dx.doi.org/10.1098/rsif.2014.0904 or via http://rsif.royalsocietypublishing.org.

THE ROYAL SOCIETY PUBLISHING

Flexibility of bacterial flagella in external shear results in complex swimming trajectories

M. Tournus[1], A. Kirshtein[1], L. V. Berlyand[1] and I. S. Aranson[2,3]

[1]Department of Mathematics, Pennsylvania State University, University Park, PA 16802, USA
[2]Materials Science Division, Argonne National Laboratory, 9700 S. Cass Avenue, Argonne, IL 60439, USA
[3]Engineering Sciences and Applied Mathematics, Northwestern University, 2145 Sheridan Road, Evanston, IL 60202, USA

Many bacteria use rotating helical flagella in swimming motility. In the search for food or migration towards a new habitat, bacteria occasionally unbundle their flagellar filaments and tumble, leading to an abrupt change in direction. Flexible flagella can also be easily deformed by external shear flow, leading to complex bacterial trajectories. Here, we examine the effects of flagella flexibility on the navigation of bacteria in two fundamental shear flows: planar shear and Poiseuille flow realized in long channels. On the basis of slender body elastodynamics and numerical analysis, we discovered a variety of non-trivial effects stemming from the interplay of self-propulsion, elasticity and shear-induced flagellar bending. We show that in planar shear flow the bacteria execute periodic motion, whereas in Poiseuille flow, they migrate towards the centre of the channel or converge towards a limit cycle. We also find that even a small amount of random reorientation can induce a strong response of bacteria, leading to overall non-periodic trajectories. Our findings exemplify the sensitive role of flagellar flexibility and shed new light on the navigation of bacteria in complex shear flows.

1. Introduction

Bacteria are among the oldest and simplest living organisms on the Earth. Bacterial activity influences the planets environmental dynamics in multiple ways, from maintaining soil structure to controlling the biochemistry and photosynthetic productivity of the oceans [1]. To search for food or populate new territories, bacteria often migrate en mass over large distances. This collective behaviour is known as swarming motility. Besides many obvious evolutionary advantages, collective behaviour appears to be also an effective strategy to prevail against antibiotics [2].

The flow produced in dense bacterial colonies in the course of swarming can be very complex because of the interaction between the bacteria and the fluid [3–7]. While the flow might visually resemble the turbulent motion emerging in rapidly stirred fluids, there is a fundamental difference: in hydrodynamic turbulence, the mechanical energy is injected at the macroscopic scale, e.g. by stirring the liquid. By contrast, in 'bacterial turbulence', the energy is injected at the microscopic scale by the rotation of helical bacterial flagella, which makes its physical properties deeply distinguished from the turbulent flow of liquid. In particular, the scale of large vortices generated by the collective bacterial locomotion does not depend on the energy injection rate [5,6]. This complex phenomena, arising owing to the intricate interplay between fluid motion and bacterial motility, are difficult to characterize experimentally. Despite significant recent progress in modelling of bacterial collective behaviour [8–11], a predictive model that describes multiple aspects of bacterial turbulence [12] has not emerged to date.

Many bacteria use rotating helical flagella for motility and for periodic reorientation, e.g. in response to chemical gradients (chemotaxis) [13]. Peritrichously flagellated bacteria, such as common *Bacillus subtilis* or *Escherichia coli* have

multiple flagellar filaments distributed over its entire bacterial body. In the course of swimming, the filament bundles are spun together. However, bacteria unbundle the filaments and tumble, leading to abrupt reorientation. The transition between the two phases (coiled and unbundle) is triggered by the reversal of a driving motor torque [14]. The flagellar filaments are typically, at least, twice longer than the bacterial body, and are very flexible, suggesting that they can be easily deformed either by the external shear flow or by the flows of other bacteria. In combination with self-propulsion, the bending of flagella could result in a significant effect on bacterial rheotaxis, i.e. a propensity of microorganism to turn into an oncoming current. It was shown, e.g. that uniflagellated bacteria exploit flagella buckling to change direction [15,16]. In addition, flagellum flexibility possibly affects the rheotactic behaviour of sperm cells [17–19].

Recently, the trajectories of self-propelled ellipsoidal rigid swimmers in a two-dimensional Poiseuille flow have been explored. Because the proximity of the boundary can significantly affect bacterial rheotaxis [20,21], the swimmer is assumed to stay far enough from the walls to exclude those interactions. The propulsion force enables the swimmer to move across the streamlines. The main result is that a self-propelled swimmer in a two-dimensional channel exhibits periodic stable oscillations around the centreline [22,23]. These periodic trajectories are strongly influenced by random reorientations (tumbling) [24] and the proximity of rigid walls [25,26]. Bacterial transport appears to be suppressed in shear Poiseuille flow, leading to the depletion of swimmers at the centre of the channel [27]. However, the response of bacterial flagella to an applied shear remains poorly understood.

A variety of specific models for helical flagellum have been derived and studied numerically. The pioneering work in that direction is due to Taylor [28], who derived from first principles the flow around a moving helix, calculated the associated force and torque and determined thereby the motion of the helix attached to a large body. In order to understand the propulsion, Purcell [29] examined the linear relationships between forces and torques and between translational and angular velocities of helical objects. Specific models were developed for microswimmers. For example, the rotational dynamics of a superhelix towed in a Stokes fluid was studied in reference [30], and a recent review can be found in Jung *et al.* [31].

It is also important to distinguish between different mechanisms leading to the alignment and reorientation of microswimmers. Some are due to biological mechanisms, such as chemotaxis [13], whereas others originate owing to pure hydrodynamic effects, as a combined effect of the surrounding fluid flow and the specific shape of the body considered. Here, we focus on the latter mechanisms. There is also a significant body of works dealing with the response of microswimmers to an external shear flow (rheotaxis), we mention just a few for review. The study was pioneered in Bretherton & Rotshchild [17] who pointed out that spermatozoa tend to align in the flow direction, and that this phenomenon is purely owing to passive hydrodynamic effects. In Kessler [32], the gyrotaxis effect in biflagellated swimming algae was described. Karp-Boss *et al.* [33] demonstrated that the differences in drag forces between body and flagella lead to preferential alignment with the flow. Recent experiments suggest that rheotaxis may significantly affect the navigation of mammalian sperm cells [18,19]. The non-trivial rheotactic response of *B. subtilis* bacteria owing to chirality of flagella was predicted in Marcos *et al.* [31].

Here, in order to examine the complex response of bacteria in an external shear, we model the swimmer as a flexible entity consisting of a rigid ellipsoidal body attached to a flexible flagellum. The trajectory of the swimmer is represented by the centre of mass of the body. To simplify the analysis and exclude side wall effects, we consider bacteria swimming in wide channels. Using elastic slender body dynamics in Stokes flow, we have shown that bacteria can exhibit complex trajectories owing to the combined effects of flagellar flexibility and self-propulsion. This behaviour is fundamentally different from that predicted for passive ellipsoidal particles [34] that move along streamlines and whose orientation is described by Jeffery orbits [22]. We have examined the behaviour of bacteria in two external shear flows: planar shear between two flat walls moving in opposite directions and two-dimensional Poiseuille flow realized in long flat channels. We have shown that, in the case of planar shear flow, the bacteria execute periodic orbits, with both the period and the amplitude determined by the shear rate, the shape of the swimmer and the flexibility of the flagella. For the case of Poiseuille flow, we have found that for a realistic range of the parameter values, the swimmer migrates towards the centreline of the channel and swims against the flow. Moreover, for softer flagella, our analysis indicates a different trend: the swimmer executes a periodic motion—a limit cycle. The amplitude of the oscillations around the centreline depends on the flexibility of the flagellum. We have also found that the occasional tumbling of bacteria may have a profound effect on the bacterial swimming trajectories owing to the complex interplay between flagellar flexibility and self-propulsion. In particular, we have found that tumbling can result in long non-periodic excursions of the bacteria, mediated by periods of steady swimming along the centreline.

Throughout this paper, we highlight the difference between passive ellipsoid particles [34], active fixed shape ellipsoidal swimmers [22], flagellated non-motile objects (e.g. dead bacteria) and flagellated self-propelled swimmers.

2. Model

2.1. Physical framework

Our main hypothesis is that, via its non-trivial coupling between the body orientation and self-propulsion, a flexible flagellum can significantly affect bacterial swimming trajectories and possibly the rheological property of the suspension [35–37]. We consider a microswimmer in a viscous fluid constituted of an ellipsoidal body linked to a flexible thin rod (flagellum) to explore its behaviour in a Poiseuille flow and planar shear flow. For the sake of simplicity, we replace the helicoidal flagellum by a thin rod. In addition, we neglect effects associated with the counter-rotation of the bacterial body [38]. The self-propulsion is implemented via a tangential force density (traction) distributed uniformly along the rod.

In our model, the geometrical and physical properties we take into account are the length of the flagellum, its propulsion–force and its elasticity.

The bacterial body on a local shear flow undergoes a rotation described by the classical Jeffery equations [34], and is rigidly attached to a flagellum of length L (figure 1). We derive the equation of motion of the flagellum in the framework of slender body theory in the Stokes flow

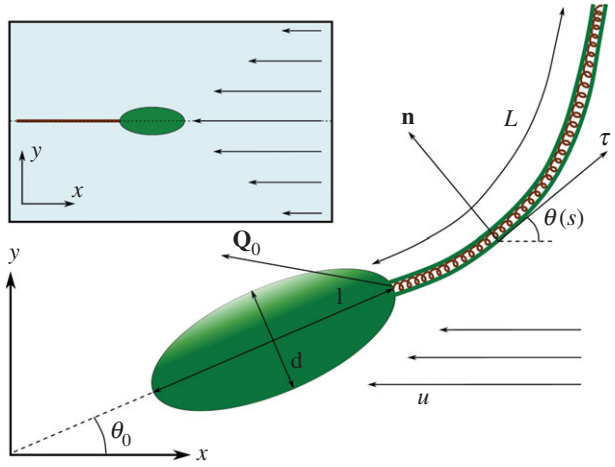

Figure 1. Schematic of the swimmer (body + flagellum). Inset: limiting configuration of the swimmer in Poiseuille flow (on the centreline, resisting the flow). (Online version in colour.)

approximation [39]. A somewhat similar derivation is performed in reference [40] for a free one-armed-swimmer modelled as a slender elastica (not attached to another body), which deforms under the effect of external magnetic torques in a Stokes flow. The novelty of our model lies in the interplay between the flexibility of the flagellum described by the slender elastica, self-propulsion and external shear flow. For the sake of simplicity, we consider that the attachment of flagella filaments to the bacterial body is rigid.[1] We also assume that the microswimmer does not affect the surrounding fluid. In order to exclude wall effects, we consider swimming in wide channels where hydrodynamic and steric interactions with the walls are negligible.

2.2. Mathematical model

The key ingredient of our model is the classical Jeffery equation (for the body) modified by an additional torque term (coming from the flagellum). This term is determined via coupling the Jeffery's orbits with a corresponding nonlinear fourth-order equation for the flagellum derived from basic physical principles. The flow is assumed to be parallel to the x-axis and its velocity vector is $u(y)\mathbf{e_x}$. Here, we summarize the model in dimensionless form (see §5.1).

Because the bacterial body is modelled by a rigid ellipsoid, we describe its motion by a Jeffery equation [34] with parameter β, the Bretherton constant of the body ($\beta = 0$ for needles and 1/2 for spheres), where the shear rate is taken to be the flow rate $u'(y^h)$ at the centre of the ellipsoid (y^h is the y-coordinate of the centre of mass of the ellipsoid, and the fluid velocity does not depend on x). We add an additional term N_0 corresponding to the normal internal stress owing to the flagellum. The modified Jeffery equation is written as

$$\left.\begin{aligned} &\frac{\mathrm{d}\theta_0}{\mathrm{d}t} = -u'(y^h)((1-\beta)\sin^2\theta_0 + \beta\cos^2\theta_0) + \frac{3L}{l}k_r N_0 \\ &\text{and} \quad \theta_0(0) = \theta_{0,\mathrm{in}}, \end{aligned}\right\} \tag{2.1}$$

where θ_0 is the orientation of the swimmer body (figure 1), l and L are respectively the length of the body and of the flagellum, and k_r is a ratio between the drag coefficients of the body and flagellum (end of §5.1).

The flagellum is represented by a one-dimensional elastica of bending rigidity K_b parametrized by the nondimensional arclength $0 \le s \le 1$. We denote by $\theta(s,t)$ the angle between the flagellum and the x-axis (figure 1). We denote by $\mathbf{Q}$ the integrated internal stress in the flagellum and by $\mathbf{Q}_0$ the force exerted by the flagellum on the body decomposed on the Frenet basis ($\boldsymbol{\tau}$, $\mathbf{n}$) of the flagellum as

$$\mathbf{Q} = \Lambda\boldsymbol{\tau} + N\mathbf{n}, \quad \mathbf{Q}_0 = \Lambda_0\boldsymbol{\tau} + N_0\mathbf{n}. \tag{2.2}$$

The equations describing the shape and motion of the flagellum are derived from the balances of forces and internal torques (see Methods, equations (5.3) and (5.5)). The forces taken into account are the fluid friction force (proportional to the relative velocity between the flagellum and the fluid according to resistive force theory) and the propulsion force, generated by an internal motor. The force density F_p is assumed constant along the flagellum. Typical value for the total force is about 1 pN, and length of the flagellum is about 10 µm, so the force density F_p is of the order of 0.1 µN m^{-1}. The balance of forces provides a vectorial relation decomposed on the Frenet basis. Substituting balance equations into geometrical identities (see Methods, equations (5.10)), we obtain two scalar equations for the angle θ and stress Λ.

$$\begin{aligned} \frac{\partial^2\Lambda}{\partial s^2} = &\frac{1}{\alpha}\Lambda\left(\frac{\partial\theta}{\partial s}\right)^2 - K_b\left(\frac{\partial^2\theta}{\partial s^2}\right)^2 - \frac{u'(y)}{2}\sin(2\theta) \\ &- \frac{(\alpha+1)}{\alpha}K_b\frac{\partial^3\theta}{\partial s^3}\frac{\partial\theta}{\partial s}, \quad t \ge 0,\ 0 \le s \le 1 \end{aligned} \tag{2.3}$$

and

$$\begin{aligned} \frac{\partial\theta}{\partial t} = &-\frac{K_b}{\alpha}\frac{\partial^4\theta}{\partial s^4} + \left(\frac{1}{\alpha}\Lambda + K_b\left(\frac{\partial\theta}{\partial s}\right)^2\right)\frac{\partial^2\theta}{\partial s^2} \\ &+ \left(\frac{\alpha+1}{\alpha}\frac{\partial\Lambda}{\partial s} + F_p\right)\frac{\partial\theta}{\partial s} - u'(y)(sin^2(\theta)), \\ &t > 0,\ 0 \le s \le 1,\ \theta(s,\ 0) = \theta_{in}(s) \end{aligned} \tag{2.4}$$

where α is a drag anisotropy factor taking into account the shape of the flagellum.

The physical hypotheses included in equations (2.3) and (2.4) are the inextensibility and the elasticity of the flagellum (see Methods, equations (5.4) and (5.9)).

Equations (2.3) and (2.4) come with a set of boundary conditions, encoding the fact that the end of the flagellum is free at $s = 1$,

$$\frac{\partial\theta}{\partial s}(1,t) = \frac{\partial^2\theta}{\partial s^2}(1,t) = \Lambda(1,t) = 0, \tag{2.5}$$

and the interface between the body and the flagellum is rigid

$$\theta(0,t) = \theta_0(t), \qquad \Lambda(0,t) = \Lambda_0(t). \tag{2.6}$$

The balance of internal torques combined with rigid attachment between the body and the flagellum provides the expression of N_0

$$N_0(t) = -K_b\frac{\partial^2\theta}{\partial s^2}(0,t). \tag{2.7}$$

Another consequence of rigid attachment is the equality of the velocity at the interface body–flagellum. This vectorial equality provides directly two scalar equations, corresponding to the tangential part

$$k_r\Lambda_0 = \frac{\alpha}{L}(u(y(0)) - u(y^h))\cos(\theta_0) + \frac{\partial\Lambda}{\partial s} + F_p - \frac{\partial\theta}{\partial s}N_0, \tag{2.8}$$

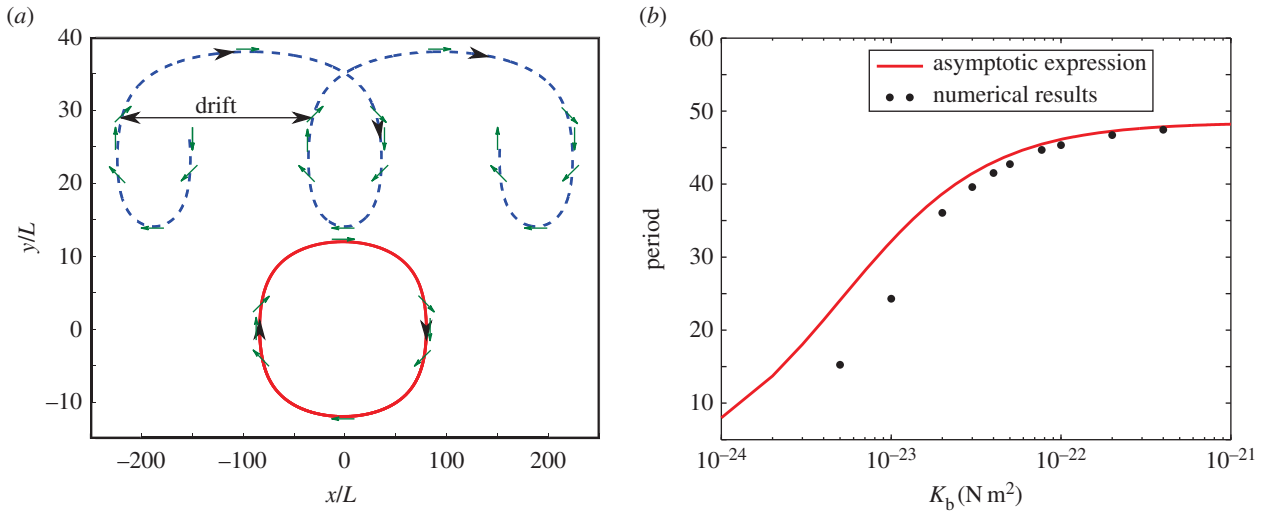

Figure 2. (*a*) Trajectories of the self-propelled swimmer in a planar shear flow for two different initial positions. Green arrows indicate the orientation $\theta_0(t)$ of the swimmer body. (*b*) Dependence of the rotation period on K_b, where K_b is the bending stiffness. The red line is the period extracted by formula (3.1). The dots are corresponding numerical results. Other parameters are taken as written in table 1. For comparison, the rotation period of a similar non-flagellated swimmer is about 23 s. (Online version in colour.)

and to the normal part of the velocity equality.

$$\left(\frac{\alpha}{\alpha_h}+\frac{3\alpha}{2}\right)k_r N_0 = -\frac{\alpha}{L}\sin(\theta_0)(u(y(0))-u(y^h)) + \frac{\alpha l}{2L}u'(y)[(1-\beta)\sin^2(\theta_0)+\beta\cos^2(\theta_0)] + \left[-K_b\frac{\partial^3\theta}{\partial s}+\frac{\partial\theta}{\partial s}\Lambda\right], \quad (2.9)$$

These two last algebraic equations only hold at $s = 0$.

To close the system, because the fluid velocity and thus the shear rate ($u'(y)$) may depend on swimmer coordinate y, we need to localize the swimmer. The y-coordinate of the body satisfies the following ordinary differential equation, similar to [23]

$$\left.\begin{aligned}&\frac{dy^h(t)}{dt} = k_r\Lambda_0(t)\sin(\theta_0(t)) + \frac{k_r}{\alpha_h}N_0(t)\cos(\theta_0(t))\\ &\text{and}\quad y^h(0) = y_0^h.\end{aligned}\right\} \quad (2.10)$$

and the position along the flagellum follows from geometrical considerations

$$\left.\begin{aligned}&\frac{\partial y(s,t)}{\partial s} = \sin(\theta(s,t))\\ &\text{and}\quad y(0,t) = y^h(t)+\frac{l}{2L}\sin(\theta_0(t)).\end{aligned}\right\} \quad (2.11)$$

The x-coordinates are not needed; however, their expression is provided in the Methods section, because they are used to plot the trajectories.

3. Results

Here, the model is studied numerically for two types of shear flows: a planar shear (linear velocity profile) and a Poiseuille flow (parabolic velocity profile). The equations for the flagellum, (2.3) and (2.4), are solved using a centred finite difference scheme on a uniform grid (approx. 100 point per micrometre on the flagellum and 10^{-2} s time step). In (2.4), the fourth- and second-order derivatives are taken implicitly, which still allows for the resolution of the scheme without iterations. We compute N_0 from the boundary condition and substitute its value into (2.1), which we solve with the forward Euler scheme. The numerical scheme is implemented in C++. See the electronic supplementary material.

3.1. Planar shear flow

In a planar shear flow, we compare the outcome of the numerical study with a theoretical result derived in the asymptotic limit of large bending stiffness K_b of the (rigid) flagellum. The fluid speed in planar shear flow is given by

$$u(y) = \gamma y. \quad (3.1)$$

We observe periodic trajectories (figure 2). When starting close to the centreline, the trajectory is closed (figure 2*a*). However, when starting on the upper part of the channel, there is a drift towards the right after one period, because the swimmer spends more time in the upper part of the channel than in the lower part. The value of the drift linearly depends on the y-initial position and vanishes when starting at $y = 0$ (see electronic supplementary material, videos S1–S3). For analysis, we linearize equations (2.1), (2.3)–(2.9) around the state given by $K_b \to \infty$, and perform a multiscale perturbation method.

From (2.3) to (2.9), in the limit of large K_b, the evolution of the bacterial body angle is given asymptotically by

$$\theta_0^0(t) = \arctan\left[\sqrt{\frac{b}{1-b}}\tan\left(t\sqrt{b(1-b)}\left(1+\frac{c}{K_b b}\right)\right)\right]. \quad (3.2)$$

Here, b and c are geometrical constants, which only depend on L, l, α, α_h, k_r and β (see the electronic supplementary material).

Equation (3.1) describes how the period of the body angle θ^0 depends on the bending stiffness K_b. For large bending stiffnesses, the body rotates according to the Jeffery equation with parameter $b < \beta$. As expected, the effective aspect ratio of the flagellated swimmer is larger than that of the non-flagellated one. The flagellum amplifies the contrast between slow rotation (swimmer parallel to the flow) and fast rotation (swimmer perpendicular to the flow). The relation given by equation (3.2) as well as the corresponding numerical

solution is plotted in figure 2*b*, using the values established in the literature for *B. subtilis*. The result shows that the period of the body rotation decreases when the flagellum becomes softer (smaller bending stiffness). As expected, in the limit of large K_b, there is a good agreement between the asymptotic analysis and numerics.

The decrease of the rotation period with the decrease in bending stiffness can be understood as follows. A softer flagellum on average bends more than a rigid one. As a result, a swimmer with a bent flagellum has an effectively smaller aspect ratio than with a more rigid one. In turn, the rotation period decreases with the increase in aspect ratio.

Thus, in a planar shear flow, as for non-flagellated swimmers [34], the trajectories of flagellated swimmers are periodic, and the period is mainly determined by the elasticity of the flagellum: the softer the flagellum, the smaller the period.

Dependence of the period on the flagellum length can be thought as a competition of two effects. On the one hand, a longer flagellum increases the effective aspect ratio of the flagellated swimmer. On the other hand, a longer flagellum is easier to bend. Numerical results show that the period has a local maximum when $L \approx 9 \times 10^{-6}$ m (with other parameters as written in table 1).

Let us point out that the shape of the flagellum strongly depends on K_b and that a buckling instability occurs up to a threshold which is about a hundred times smaller than the realistic value $K_b = 3 \times 10^{-23}$ N m^2, see the electronic supplementary material.

3.2. Poiseuille flow

The majority of experiments [19,20,27] are performed in a rectangular channel of width w (or in circular channel of radius r_0). In the planar geometry, assuming no-slip boundary conditions, the x-component of fluid velocity has the following parabolic profile

$$u(y) = p(y^2 - \frac{w^2}{4}), \tag{3.3}$$

where p is the applied pressure normalized on the dynamic viscosity of suspending liquid.

First, we investigate the stability of steady-state swimming along the centreline. In reference [23], the trajectories of a self-propelled ellipsoidal swimmer (with point–force propulsion) in a Poiseuille flow are shown to be periodic. The presence of the flagellum makes our system more difficult to deal with, nevertheless, in the large K_b limit the properties of the trajectories can be studied analytically. In particular, it is clear that the states $[y = 0,\ \theta = 0]$ and $[y = 0,\ \theta = \pi]$ (i.e. the swimmer with a straight flagellum swims along the centreline) are the only stationary states of the system. In the large K_b limit, the state $[y = 0,\ \theta = \pi]$ (i.e. swimming against the flow) is the only linearly stable equilibrium.

The linearized system around the stationary state $[y = 0, \theta = \pi]$ is of the form

$$\left.\begin{aligned} &\frac{\mathrm{d}\theta_0(t)}{\mathrm{d}t} = -2py(t) + 3N_0(t) \\ \text{and}\quad &\frac{\mathrm{d}y(t)}{\mathrm{d}t} = \frac{F_P \cos(\pi)}{3}\theta_0(t) + \frac{\cos(\pi)}{4}N_0(t), \end{aligned}\right\} \tag{3.4}$$

Table 1. Parameter values used in the numerical simulations.

parameter	parameter value
α	2
β	0.0192
γ	0.1 s^{-1}
d	7×10^{-7} m
η_0	10^{-3} Pa s
F_p	10^{-7} N m^{-1}
K_b	3×10^{-23} N m^2
L	10^{-5} m
l	5×10^{-6} m
ζ_f	10^{-3} N s m^{-2}
ζ_h	1.6×10^{-8} N s m^{-1}
p	10^4 m^{-1} s^{-1}
w	4×10^{-4} m

where N_0 is determined by

$$\left.\begin{aligned} &\frac{\partial\theta}{\partial t}(s,t) = -\frac{K_b}{2}\frac{\partial^4\theta}{\partial s^4} - \frac{F_p}{3}(s-1)\frac{\partial^2\theta}{\partial s^2}, \\ &N_0 = -K_b\frac{\partial^2\theta}{\partial s^2}(s=0) \\ &N_0 = -\frac{\beta p}{4}y - \frac{K_b}{2}\frac{\partial^3\theta}{\partial s^3}(s=0) - \frac{F_p}{3}\frac{\partial\theta}{\partial s}(s=0) \\ \text{and}\quad &\frac{\partial\theta}{\partial s}(1,t) = \frac{\partial^2\theta}{\partial s^2}(1,t) = 0, \quad \theta(0,t) = \theta_0(t). \end{aligned}\right\} \tag{3.5}$$

We note that the second-order term in the first line of (3.5) causes a buckling instability. If there is no flagellum, i.e. $N_0 = 0$, the matrix of the linear system $\mathrm{d}/\mathrm{d}t(\theta_0, y)^T = A(\theta_0, y)^T$ is

$$A = \begin{pmatrix} 0 & -2p \\ \dfrac{-F_p\cos(\pi)}{3} & 0 \end{pmatrix}.$$

$\mathrm{Tr}(A) = 0$ and $\mathrm{Det}(A) > 0$, which means that the eigenvalues are imaginary. From (3.5), N_0 is computed as

$$N_0 = -\frac{1}{3}\left(\frac{\mathrm{d}\theta_0}{\mathrm{d}t} + \beta p y\right). \tag{3.6}$$

Substitution of (3.6) into the linear system (3.3) gives us, after straightforward computations, that $[y = 0,\ \theta = \pi]$ is stable, whereas $[y = 0,\ \theta = 0]$ is not. This is in agreement with the numerical observation that in Poiseuille flow, for large enough values of the bending stiffness, the bacteria swim opposite to the flow direction after a long period of time. The bacterium was launched at $y = 5$, with an angle $\theta_0 = 0$ (i.e. parallel to the walls) and a straight flagellum. The swimmer performs large loops, first in the upper part of the channel, then in both halves (figure 3*a*). The amplitude of the loops is decreasing with time, and at the end, the swimmer converges to the centreline of the channel and orients against the flow (figure 1 inset).

The flow strength was taken sufficiently high to avoid any collision between the swimmer and the wall. Thus, the swimmer always drifts downstream. Owing to the vorticity of the flow, the swimmer first (short time, $x \approx -10^4$ in figure 3*a*) performs a 'tumbling' motion (as defined in reference [22]),

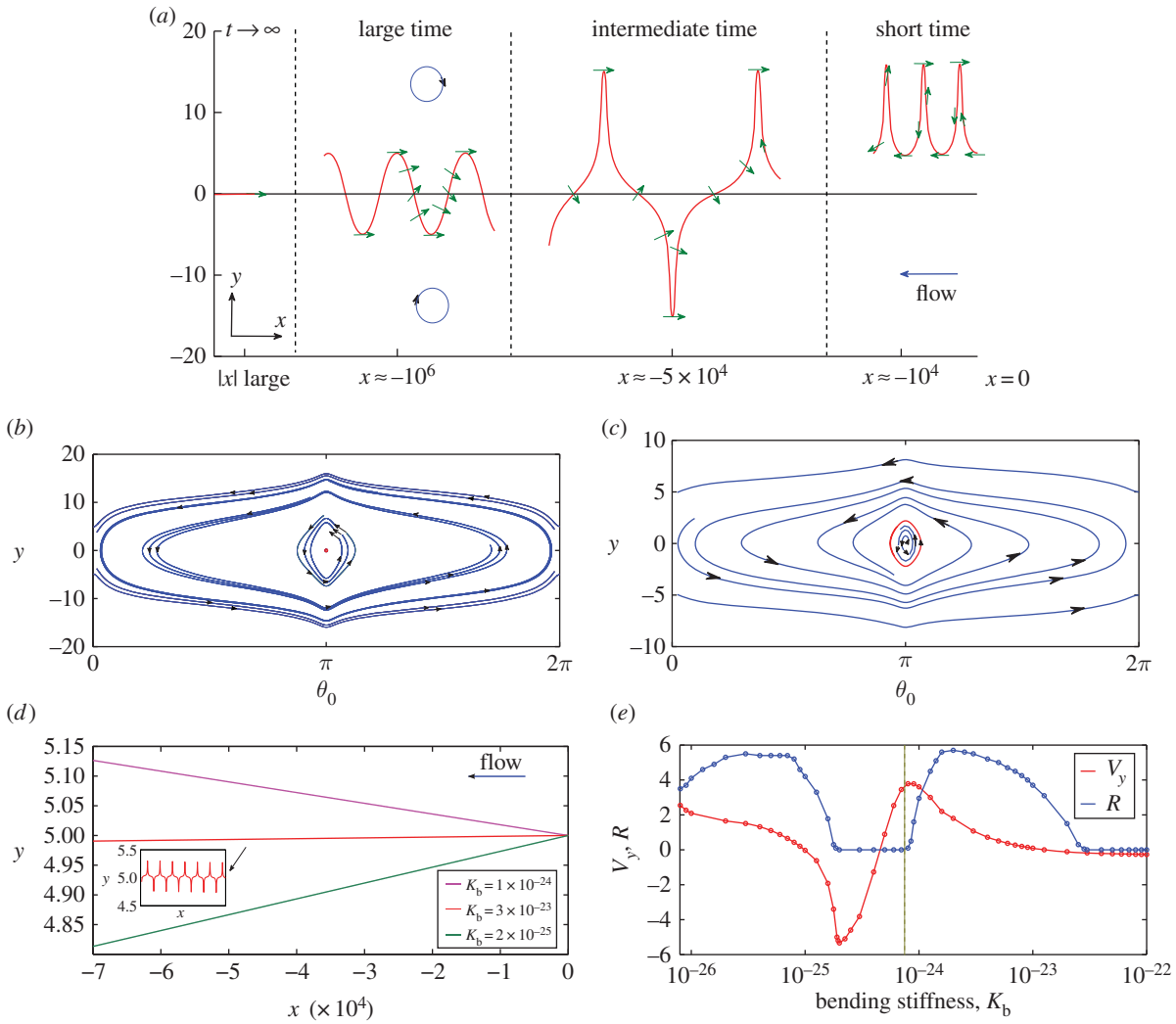

Figure 3. (*a*) Representative trajectory $(x(t), y(t))$ of the swimmer in the channel for different intervals of time, for the physical value of the bending stiffness ($K_b = 3 \times 10^{-23}$ N m^2). The arrows indicate the orientation $\theta_0(t)$ of the swimmer's body. The blue circles indicate the sign of the vorticity. (*b*,*c*) Phase portraits of the trajectories of the self-propelled swimmer. For large values of the bending stiffness, the swimmer converges towards the centre of the channel swimming against the flow (*b*), for a smaller value of the bending stiffness, there is a limit cycle (*c*). (*d*) Averaged trajectory over a period of the passive swimmer for three different bending stiffness. Depending of the bending stiffness value, there is an averaged drift towards or away from the centre. The inset corresponds to the real shape of the trajectory. The convergence is slow, so we need to consider large values on the *x*-axis (downstream). (*e*) Averaged *y* velocity of the passive swimmer $\langle V_y \rangle$ versus bending stiffness compared with the size of the limit cycle *R* versus bending stiffness for the self-propelled swimmer. Dots correspond to values given by the numerical scheme, the dotted lines are an interpolation of the dots. *R* is the maximum distance from the centre of the channel that the swimmer reaches after a long period of time (i.e. $R := \limsup_{t\to\infty} |y_0(t)|$). Except for K_b, parameter values were taken as written in table 1 and $p = 10^4$ s m^{-1}. The vertical line indicates the buckling threshold. (Online version in colour.)

i.e. the body is undergoing complete rotation, in one part of the channel and has a slight drift towards the centre of the channel.[2] Owing to this drift, after some time, the swimmer crosses the centreline. It then begins (at an intermediate time) to visit both sides of the channel, performing a 'swinging' motion (as defined in reference [22]), i.e. the body oscillates around the angle π, because the difference of vorticity between the upper and lower side of the channel prevents it from undergoing a complete rotation. However, owing to the flexibility of the flagella, the amplitude of the excursions becomes smaller and smaller, and after a long period of time, the swimmer reaches a stable stationary state, in stark contrast to the behaviour of a swimmer modelled by a rigid body without a flagellum. The equations describing the trajectory of self-propelled fixed-shape ellipsoidal swimmers have been studied in reference [23] where the authors observed two different periodic behaviours, 'tumbling' and 'swinging', depending on the *y*-coordinate of the initial position. In our case, there is a drift towards the centre of the channel owing to presence of the flagellum, which breaks the periodicity of the trajectories and allows the swimmer to switch from 'tumbling' motion to 'swinging' motion (figure 3*b*, non-closed and closed curves, respectively).

3.2.1. Heuristic argument for the convergence towards the centreline for large bending stiffness

Here, we present a simple explanation of why the swimmer converges towards the centreline owing to its flagellum flexibility in the case where the flagellum is rigid enough. Two mechanisms are responsible for the convergence towards the centre: the elastic response of the flagellum tends to displace the centre of mass of the swimmer, and the propulsion force amplifies this phenomenon.

The propulsion force amplifies the drift towards the centre. First, the convergence towards the centre is not a sole property of self-propelled swimmers. Numerical results show that our flagellated object (e.g. dead bacterium) with no propulsion force (i.e for $F_p = 0$) undergoes a slight drift towards the centre of the channel (figure 3*d*; $K_b = 3 \times 10^{-23}$ N m^2).

Under assumptions used in reference [34], a passive ellipsoid is expected to drift along the streamlines. This small drift towards the centre is negligible compared with the lift force that occurs to the nonlinear profile of the Poiseuille flow [41], which in contrast, makes the swimmer migrate away from the centre (see §5.2.1). However, for self-propelled swimmers, the migration towards the centre is amplified by the propulsion force, whereas the lift force is not.

The elastic response of the flagellum tends to displace the centre of mass of the swimmer. For large enough bending stiffness (e.g. larger than $K_b = 3 \times 10^{-23}$N m^2), there is an overall tendency of the flagellum to straighten owing to the bending rigidity described by the fourth-order term in (2.4). This phenomenon results in a net displacement of the body, for both self- and non-self-propelled swimmers, and the direction of the body displacement is the orientation of the body. The y-component of this displacement determines whether the swimmer drifts towards or away from the centre. The higher the shear rate experienced by the flagellum, the more important the vertical displacement. Because the shear rate experienced by the flagellum is higher when further from the centreline, this displacement is more important when the swimmer is oriented towards the centre.

Why convergence towards the centre does not occur in planar shear flow. The migration towards the centre is not observed in planar shear flow. The reason is the following: in a planar shear flow, whatever the orientation of the swimmer is, the shear experienced by each point of the flagellum only depends on the position of the body (because the shear rate is constant everywhere). No direction (away or towards the centre) is preferred.

3.2.2. Non-monotone dependence of the limiting behaviour on the bending stiffness

The heuristic explanation we provided above is no longer valid for small values of the bending stiffness. For the chosen value of dimensionless pressure gradient $p = 10^4$ and smaller bending stiffness $K_b = 10^{-24}$ N m^2 (representative value for *B. subtilis* is $K_b = 3 \times 10^{-23}$ N m^2), the self-propelled swimmer no longer drifts towards the centre, but instead converges towards a limit cycle (figure 3*c*), where the swimmer swings around the centreline. When further decreasing the bending stiffness ($K_b = 2 \times 10^{-25}$ N m^2), the behaviour is again similar to $K_b = 3 \times 10^{-23}$ N m^2. This suggests that the behaviour of the system is non-trivial. It has been observed numerically that depending on the bending stiffness of the flagellum, the non-self-propelled flagellated object ($F_p = 0$) can either drift towards the walls or towards the centre (figure 3*d*, $K_b = 10^{-24}$ and $K_b = 9 \times 10^{-24}$ N m^2, respectively). In addition, we observed that the self-propelled swimmer either converges towards a stable stationary state or a limit cycle. For different bending stiffness values, the y-averaged velocity of a non-self-propelled object is plotted in figure 3*e*. If the averaged velocity is negative (e.g. $K_b \geq 3 \times 10^{-23}$ N m^2), the non-self-propelled swimmer tends to reach the centre of the channel. If the averaged velocity is positive (e.g. $K_b = 10^{-24}$ N m^2), the swimmer migrates away from the centre. Clearly, there is a strong correlation between the size of limit cycle R for the self-propelled swimmer and average y velocity $\langle V_y \rangle$ of the non-motile flagellated body (figure 3*e*). Ranges of the bending stiffness where the averaged velocity of the non-self-propelled object is negative correspond approximately to ranges where the self-propelled swimmer converges towards the centre (size of the limit cycle = 0). Conversely, ranges of the bending stiffness where the averaged velocity of the non-motile body is positive correspond to ranges where the self-propelled swimmer converges towards a limit cycle. It means that the bending stiffness value determines the qualitative behaviour of the swimmer. When decreasing F_p, but staying close to the physical value (50%), the curve R is slightly shifted on the left and has a smaller amplitude. The pressure gradient of the flow p, on the other hand, does not affect qualitatively the long time behaviour of the swimmer, but it has a quantitative effect: the ranges of values of K_b where the swimmer converges towards the stationary state or the limit cycle are the same, whatever p. However, increasing p accelerates the convergence towards the steady state, and reduces the size R of the limit cycle.

3.2.3. Random reorientation (tumbling events)

For large values of the bending stiffness, the swimmer asymptotically converges towards the centreline. However, tumbling, which is in that context an abrupt reorientation of a swimmer, may destabilize the steady state. To verify this assumption, we incorporated random reorientation in our model. A good approximation to the probability distribution of tumbling events in time is a Poisson distribution [42]. It implies that the total number of tumbles occurring between time s and t is a Poisson random variable with parameter $\lambda_r(t - s)$, where λ_r is the intensity of the Poisson law. The Poisson process determines the instant of reorientation, and the angle changes according to the uniform distribution on $[0,2\pi]$. The flagellum reorients as well with the same angle. With random reorientation present, the relaxation towards the steady state no longer occurs. We display in figure 4 two selected time intervals at which tumbling occurs. Recall that the fluid is moving is the negative direction, so that each plot has to be read from right to left. On plots (*a*,*b*), the swimmer undergoes a 'swing' when the tumble event occurs. If no random reorientation occurs, the angle of the body would have relaxed towards π- and the y-amplitude of the trajectory would have decreased to $y = 0$. The tumble event reorients the swimmer and makes it switch to another point of the phase portrait (figure 3*b*). In figure 4*a*, after the tumble event the swimmer is still 'winging', but the amplitude of the trajectory has increased. On plots (*c*,*d*), the swimmer was also undergoing a 'swinging' motion when the tumble event occurs. The new orientation of the swimmer is $3\pi/2$, and the motion switches to a 'tumbling' motion (i.e. the swimmer is undergoing a complete rotation) on the lower part of the channel. Thus, the qualitative behaviour of the swimmer may drastically change owing to a relatively rare random reorientation, eliminating the overall convergence to the centreline.

4. Conclusion

Based on partial differential equations, we introduced a nonlinear model that couples the body motion of a swimmer with a flexible flagellum attached to it. Linear asymptotic analysis of this model for planar shear flow shows how classical Jeffery orbits change owing to the flagellum. In particular, we found the dependence of the body rotation period on the flagellum bending stiffness. Next, we performed a numerical analysis of this model in Poiseuille flow and made several important observations. First, the model exhibits non-periodic trajectories owing to the presence of the

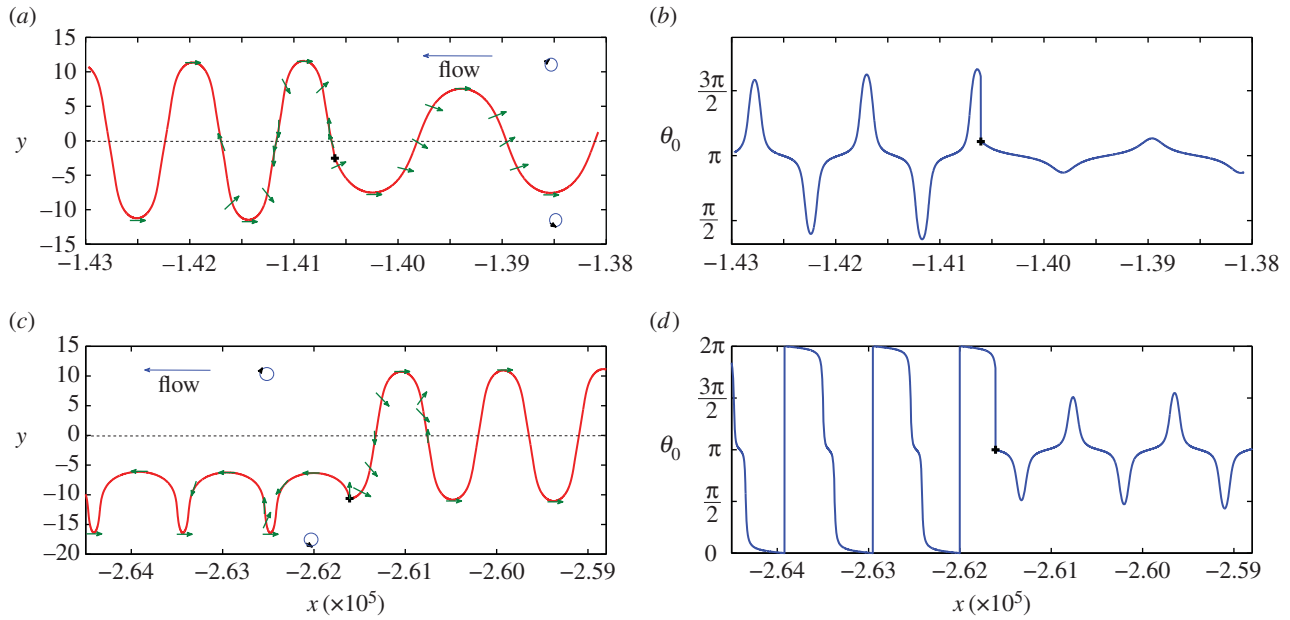

Figure 4. (*a*,*c*) Trajectories of the self-propelled swimmer in the (*x*,*y*) space for two selected time intervals. The fluid flows from the right to the left and the blue circles indicate the sign of the vorticity. Green arrows indicate the orientation $\theta_0(t)$ of the swimmer body. The symbol '+' shows the tumbling events. (*b*,*d*) Orientation θ_0 of the swimmer as a function of *x*. The intensity of the Poisson process is taken to be 0.1 min, which means that a tumbling event occurs in average every 10 min. Other parameters are taken as written in table 1. (Online version in colour.)

flagellum. This stands in contrast to classical periodic trajectories for the Jeffery equation for passive particles, and even more striking, when compared with periodic trajectories for fixed-shape active swimmers [23] that are self-propelled but have no flagellum. Second, we observe that the long time behaviour of our system is non-monotonic as a function of bending stiffness. Namely, for large bending stiffness, the system reaches a steady state. When bending stiffness is decreased, it converges towards a limit cycle. Further decrease in the bending stiffness results in convergence towards a steady state again. Finally, we observe that even a small amount of random tumbling events drastically affect the above described behaviour.

5. Methods

5.1. Derivation of the equations of motion

5.1.1. The flexible flagellum

To derive the equations of motion, we employ resistive force theory and theory of the elasticity of a slender body. We use the arclength $0 \le s \le L$ to parametrize the flagellum. We denote by $\theta(s, t)$ the angle between the flagellum and the *x*-axis (figure 1). We also introduce local tangent, normal and binormal vectors

$$\boldsymbol{\tau} = \begin{pmatrix} \cos(\theta) \\ \sin(\theta) \\ 0 \end{pmatrix}, \quad \mathbf{n} = \begin{pmatrix} -\sin(\theta) \\ \cos(\theta) \\ 0 \end{pmatrix}, \quad \mathbf{b} = \begin{pmatrix} 0 \\ 0 \\ 1 \end{pmatrix},$$

and write the velocity of the point of the flagellum as

$$\mathbf{v} = v_\tau \boldsymbol{\tau} + v_n \mathbf{n}. \tag{5.1}$$

Denoting by $\mathbf{Q}$ the integrated internal stress in the flagellum and by $\mathbf{Q}_0$ the force exerted by the flagellum on the body

$$\mathbf{Q} = \Lambda \boldsymbol{\tau} + N\mathbf{n}, \quad \mathbf{Q}_0 = \Lambda_0 \boldsymbol{\tau} + N_0 \mathbf{n}. \tag{5.2}$$

In the framework of the resistive force theory, the force exerted by the fluid on the flagellum is proportional to the relative velocity between the flagellum and the fluid. The force balance states that the divergence of the internal stress is equal to the external force applied to the flagellum, yielding the following relations

$$\frac{\partial}{\partial s}(\Lambda \boldsymbol{\tau} + N\mathbf{n}) = \zeta_\mathrm{f}(v_\tau - u(y)\cos\theta)\boldsymbol{\tau} + \alpha\zeta_\mathrm{f}(v_n + u(y)\sin\theta)\mathbf{n} - F_\mathrm{p}\boldsymbol{\tau}. \tag{5.3}$$

Here, F_p is the propulsion force density generated by the flagellum. The parameter ζ_f is the drag coefficient of the flagellum, and α is a drag anisotropy factor owing to the shape of the flagellum. Following Roper *et al.* [40], we set $\zeta_\mathrm{f} = 2\pi\eta_0/\log(L/D)$, where η_0 is the viscosity of the fluid, and $\alpha = 2$ (slender body). The elasticity of the flagellum is represented by the constitutive relation

$$\mathbf{M} = K_\mathrm{b}\boldsymbol{\kappa}\mathbf{b}, \tag{5.4}$$

where κ is the local flagellum curvature, defined by $\kappa = \partial\theta/\partial s$. The balance of internal torques gives

$$\frac{\partial \mathbf{M}}{\partial s} + \boldsymbol{\tau} \times \mathbf{Q} = 0, \tag{5.5}$$

which combined with (5.4) gives an expression of the normal component of the internal stress

$$N = -K_\mathrm{b}\frac{\partial^2\theta}{\partial s^2}. \tag{5.6}$$

The force balance vector relation (5.3) can be separated into the tangential and normal parts

$$\zeta_\mathrm{f} v_\tau = \zeta_f u(y)\cos\theta + \frac{\partial \Lambda}{\partial s} + F_p - \kappa N \quad \text{and} \quad \alpha\zeta_\mathrm{f} v_n = -\alpha\zeta_\mathrm{f} u(y)\sin\theta + \frac{\partial N}{\partial s} + \kappa\Lambda. \tag{5.7}$$

We derive the equations for Λ and θ, using the geometrical Frenet relations

$$\frac{\partial \boldsymbol{\tau}}{\partial s} = \boldsymbol{\kappa}\mathbf{n}, \quad \frac{\partial \mathbf{n}}{\partial s} = -\boldsymbol{\kappa}\boldsymbol{\tau},$$

yielding

$$\frac{\mathrm{d}\boldsymbol{\tau}}{\mathrm{d}s} = \frac{\mathrm{d}v}{\mathrm{d}s} = \left(\frac{\partial v_\tau}{\partial s} - \kappa v_n\right)\boldsymbol{\tau} + \left(\frac{\partial v_n}{\partial s} + \kappa v_\tau\right)\mathbf{n}. \tag{5.8}$$

The inextensibility of the flagellum can be cast in the form

$$\frac{\mathrm{d}\boldsymbol{\tau}}{\mathrm{d}s} = \left(\frac{\partial\theta}{\partial t}\right)\mathbf{n} \tag{5.9}$$

By identifying the terms in (5.8) and (5.9), we obtain

$$\frac{\partial v_\tau}{\partial s} = \kappa v_n, \quad \frac{\partial\theta}{\partial t} = \frac{\partial v_n}{\partial s} + \kappa v_\tau, \tag{5.10}$$

which gives us the following equations on Λ and θ

$$\begin{aligned}\alpha\frac{\partial^2\Lambda}{\partial s^2} = {} & \left(\frac{\partial\theta}{\partial s}\right)^2\Lambda - \alpha K_\mathrm{b}\left(\frac{\partial^2\theta}{\partial s^2}\right)^2 - \frac{\alpha}{2}u'(y)\zeta_\mathrm{f}\sin(2\theta) \\ & - \frac{\partial\theta}{\partial s}(\alpha+1)K_\mathrm{b}\frac{\partial^3\theta}{\partial s^3},\end{aligned} \tag{5.11}$$

$$\begin{aligned}\alpha\zeta_\mathrm{f}\frac{\partial\theta}{\partial t} = {} & -K_\mathrm{b}\frac{\partial^4\theta}{\partial s^4} + \left(\Lambda + \alpha K_\mathrm{b}\left(\frac{\partial\theta}{\partial s}\right)^2\right)\frac{\partial^2\theta}{\partial s^2} \\ & + \left((\alpha+1)\frac{\partial\Lambda}{\partial s} + \alpha F_\mathrm{p}\right)\frac{\partial\theta}{\partial s} - u'(y)\alpha\zeta_\mathrm{f}\sin^2(\theta).\end{aligned} \tag{5.12}$$

Boundary conditions. The flagellum end is free at $s = L$, and the connection between the body and the flagellum is rigid. It gives the set of boundary conditions

$$\frac{\partial\theta}{\partial s}(L,t) = \frac{\partial^2\theta}{\partial s^2}(L,t) = \Lambda(L,t) = 0 \tag{5.13}$$

and

$$\theta(0,t) = \theta_0(t), \quad \Lambda(0,t) = \Lambda_0(t), \tag{5.14}$$

where $\theta_0(t)$ and $\Lambda a_0(t)$ are respectively the angle of body with the x-axis and the tangential internal stress at the interface body/flagellum. We add the condition

$$N_0(t) = -K_\mathrm{b}\frac{\partial^2\theta}{\partial s^2}(0,t), \tag{5.15}$$

which is a consequence of the rigid connection between the body and the flagellum, combined with (5.6).

5.1.2. Motion of the bacterial body

The motion of passive rigid ellipsoids is described by the Jeffery equation. In the first-order approximation, the flow around the ellipsoid can be treated as a planar shear flow. We describe the bacterial body motion by the Jeffery equations, where the shear rate is taken to be the flow rate at the centre of the ellipsoid. We add an additional term corresponding to the normal internal stress coming from the flagellum. The modified Jeffery equation is written as

$$\begin{aligned}\frac{\mathrm{d}\theta_0}{\mathrm{d}t} = {} & -u'(y^h)\left(\frac{l^2}{l^2+d^2}\sin^2\theta_0(t) + \frac{d^2}{l^2+d^2}\cos^2\theta_0(t)\right) \\ & + \frac{l}{2\zeta_\mathrm{r}}N_0(t),\end{aligned} \tag{5.16}$$

where y^h is the y-coordinate of the centre of mass of the ellipsoid. The velocity of the body centre of mass has two components: the first comes from the flow, and the second comes from the stress of the flagellum. We neglect the perturbations produced by the body on the flow.

5.1.3. Body–flagellum interface conditions

The body makes contact with the flagellum at $s = 0$. The rigidity of the junction implies the equality of the local velocities at the contact body–flagellum. Using (5.7), the local velocities of the flagellum are expressed as

$$\left.\begin{aligned} & v_\tau(0) = u(y(0))\cos\theta + \frac{1}{\zeta_\mathrm{f}}\left[\frac{\partial\Lambda}{\partial s}(0) + F_\mathrm{p} - \kappa N_0,\right] \\ \text{and} \quad & v_n(0) = -u(y(0))\sin\theta + \frac{1}{\zeta_\mathrm{f}}\left[\frac{\partial N}{\partial s}(0) + \kappa\Lambda_0\right].\end{aligned}\right\} \tag{5.17}$$

The velocities of the body are given by

$$\left.\begin{aligned} & v_\tau^h = u(y^h)\cos\theta_0 + \frac{1}{\zeta_h}\Lambda_0 \\ \text{and} \quad & v_n^h = -u(y^h)\sin\theta_0 + \frac{1}{\zeta_h\alpha_h}N_0,\end{aligned}\right\} \tag{5.18}$$

where ζ_h is the drag coefficient of the body, $\zeta_\mathrm{h} = 2\pi\eta_0 l/\log(l/d)$, and α_h is an anisotropy drag factor, taken to be 2 (slender body approximation [40]). The tangential components of the velocities are the same, but there is an extra term for the normal velocities given that $v_n(0)$ represents the normal velocity at the flagellum–body contact, whereas $v_{n,0}$ is the normal velocity of the centre of the body which are at a distance $l/2$ of each other.

$$v_\tau(0) = v_{\tau,0}, \quad v_n(0) = v_{n,0} + \frac{l}{2}\frac{\mathrm{d}\theta_0}{\mathrm{d}t}. \tag{5.19}$$

The equalities in (5.19) holding at $s = 0$ are expressed as follows, using (5.17) and (3.18).

$$\left.\begin{aligned} & \frac{1}{\zeta_h}\Lambda_0 = \cos(\theta_0)(u(y(0)) - u(y^h)) + \frac{1}{\zeta_\mathrm{f}}\left[\frac{\partial\Lambda}{\partial s} + F_\mathrm{p} + K_\mathrm{b}\frac{\partial\theta}{\partial s}\frac{\partial^2\theta}{\partial s^2}\right] \\ \text{and} \quad & \frac{1}{\zeta_h\alpha_h}N_0 + \frac{l}{2}\frac{\mathrm{d}\theta_0}{\mathrm{d}t} = -\sin(\theta_0)(u(y(0)) - u(y^h)) + \frac{1}{\alpha\zeta_\mathrm{f}}\left[-K_\mathrm{b}\frac{\partial^3\theta}{\partial s^3} + \frac{\partial\theta}{\partial s}\Lambda\right].\end{aligned}\right\} \tag{5.20}$$

5.1.4. Expressions for the coordinates

Because the swimmer's velocity depends on the local velocity of ambient fluid, which itself depends on the y-coordinate, we express $y^h(t)$ and $y(s,t)$, the vertical position of the centre body and of the flagellum, respectively. We also study the evolution of the x-coordinate, as it is useful to describe the trajectories. Owing to geometrical considerations, the body position (x^h, y^h) satisfies the following equations

$$\left.\begin{aligned} & \frac{\mathrm{d}x^h(t)}{\mathrm{d}t} = v_{\tau,0}\cos(\theta_0(t)) - v_{n,0}(t)\sin(\theta_0(t)), \\ & \frac{\mathrm{d}y^h(t)}{\mathrm{d}t} = v_{\tau,0}\sin(\theta_0(t)) + v_{n,0}\cos(\theta_0(t)) \\ \text{and} \quad & x^h(0) = x_0^h, \quad y^h(0) = y_0^h,\end{aligned}\right\} \tag{5.21}$$

where (x_0^h, y_0^h) is the initial position of centre of mass of the body. We substitute the expressions of the tangential and normal velocities (3.18) and obtain

$$\left.\begin{aligned} & \frac{\mathrm{d}x^h(t)}{\mathrm{d}t} = u(x^h(t), y^h(t)) + \frac{1}{\zeta_h}\Lambda_0(t)\cos(\theta_0(t)) \\ & \qquad - \frac{1}{\alpha_h\zeta_h}N_0(t)\sin(\theta_0(t)), \\ & \frac{\mathrm{d}y^h(t)}{\mathrm{d}t} = \frac{1}{\zeta_h}\Lambda_0(t)\sin(\theta_0(t)) + \frac{1}{\alpha_h\zeta_h}N_0(t)\cos(\theta_0(t)) \\ \text{and} \quad & x^h(0) = x_0^h,\ y^h(0) = y_0^h.\end{aligned}\right\} \tag{5.22}$$

Table 2. Numerical values of the rescaled variables.

rescaled variable	representative value
b	5×10^{-3}
c	-0.0045
F_p	100
K_b	30
k_r	0.65
E	1

The positions of the flagellum may then be written in the form

$$\left.\begin{aligned} \frac{\partial x(s,t)}{\partial s} &= \cos(\theta(s,t)) \\ \frac{\partial y(s,t)}{\partial s} &= \sin(\theta(s,t)) \\ x(0,t) &= x^h(t) + \frac{l}{2}\cos(\theta_0(t)) \\ \text{and} \qquad y(0,t) &= y^h(t) + \frac{l}{2}\sin(\theta_0(t)). \end{aligned}\right\} \tag{5.23}$$

5.1.5. Rescaling

We first define the order of magnitude of the shear rate as γ_0. The variables are rescaled as

$$\tilde{s} = \frac{s}{L}, \quad \tilde{u} = \frac{u}{L\gamma_0}, \quad \tilde{t} = \gamma_0 t, \quad \tilde{\Lambda} = \frac{\Lambda}{\zeta_f \gamma_0 L^2},$$
$$\tilde{\Lambda}_0 = \frac{\Lambda_0}{\zeta_f \gamma_0 L^2}, \quad \tilde{N}_0 = \frac{N_0}{\zeta_f \gamma_0 L^2}, \quad \zeta_r = \frac{l^2 \zeta_h}{6},$$
$$\tilde{K}_b = \frac{K_b}{\zeta_f \gamma_0 L^4}, \quad \tilde{F}_p = \frac{F_p}{\zeta_f \gamma_0 L}, \quad k_r = \frac{L\zeta_f}{\zeta_h},$$
$$\beta = \frac{d^2}{l^2 + d^2},$$

In §2, we use these rescaled variables, but we omit the tildes to simplify the notation (table 2).

5.2. Random reorientation (tumbling)

We define T_{run} as the time between two random reorientation. If we denote by N_t the number of reorientations occurring before time t, we have

$$\mathbb{P}[(N_t - N_s) = k] = e^{-\lambda_r(t-s)} \frac{(\lambda_r(t-s))^k}{k!}, \tag{5.24}$$

where $\mathbb{P}$ is probability of the event. This causes the distribution of run duration to be exponential. Indeed, if T_{run1} is the time at which first reorientation occurs, we have

$$\mathbb{P}(T_{run1} \geq t) = \mathbb{P}(N_t = 0) = \exp(-\lambda_r t), \tag{5.25}$$

which means that the time of the first run has an exponential distribution. The parameter $1/\lambda_r$ is the expectation of T_{run} and is taken to be 10 min.

To simulate the exponential distribution, we generate a uniform random variable U using a random number generator in C++. We denote by G the inverse of the repartition function of the exponential law, namely $G(u) = -(1/\lambda_r)\ln(1-u)$, then the random variable $G \circ U$ has an exponential distribution, because

$$\mathbb{P}(G \circ U \leq t) = \mathbb{P}(U \leq F(t)) = F(t). \tag{5.26}$$

5.2.1. Effects of parabolic flow profile

In the analysis above, we neglected the effect owing to parabolic profile of the flow. In the context of a spherical particle in an unbounded flow, the lift force exerted by the fluid on a body whose centre is in y^h is of the form

$$\text{lift} = 6.46\ \eta_0 r \Delta u \frac{\sqrt{R}}{4}, \quad R = \rho u'(y^h)\frac{r^2}{\eta_0}, \tag{5.27}$$

where ρ is the ratio between the solid and the fluid density, Δu is the slip velocity of the particle (the particle velocity minus the undisturbed velocity at the particle centre) and r is the radius of the body (see [41,43]). This expression is valid only for spherical swimmers. In our case, the swimmer is close to a rod of length l. Thus, in (5.27), we replace the radius r by the effective radius, $l/2|\sin(\theta_0)|$, which corresponds to the radius seen by the fluid. This results in $\Delta u = |u(y^h + (l/2)\sin(\theta_0)) - u(y^h)| \approx |4l\sin(\theta_0)|$.

In the Poiseuille flow, assuming that $\rho = 1$, the formula becomes

$$\text{lift} = \frac{6.46}{4}\sqrt{\eta_0}\sqrt{u'(y^h)}pl^3|\sin^3(\theta_0)|\mathbf{e}_y, \tag{5.28}$$

With the order of magnitude of the parameters, lift $\approx 10^{-14}$ N, which can be neglected, in comparison with the total propulsion force $L \times F_p$, which is of the order of few pN. The model including this lift effect was implemented, and no notable change in the behaviour was observed.

Acknowledgement. The theoretical work was supported by the NIH grant 1R01GM104978-01. The simulations at Argonne and work of I.S.A. were supported by the US DOE BES, Division of Materials Science and Engineering (I.S.A.).

Endnotes

[1]An individual flagellar filament is attached to the body via a soft hook. As it was shown in Son *et al.* [16], the flexibility and buckling of the hook plays a profound role in the tumbling of uniflagellated bacteria. However, in the case of bacteria with multiple flagellar filaments distributed over the bacterial body, such as *B. subtilis*, flexibility owing to soft hook coupling is not important, because the flagella form tight bundles.

[2]Here, we distinguish 'tumbling' motion owing to vorticity of the flow from 'run-and-tumble' behaviour of bacteria owing to unbundling of flagella.

References

1. Stocker R. 2012 Marine microbes see a sea of gradients. *Science* **338**, 628–633. (doi:10.1126/science.1208929)
2. Butler MT, Wang Q, Harshey RM. 2010 Cell density and mobility protect swarming bacteria against antibiotics. *Proc. Natl Acad. Sci. USA* **107**, 3776–3781. (doi:10.1073/pnas.0910934107)
3. Dombrowski C, Cisneros L, Chatkaew S, Goldstein RE, Kessler JO. 2004 Self-concentration and large-scale coherence in bacterial dynamics. *Phys. Rev. Lett.* **93**, 098103. (doi:10.1103/PhysRevLett.93.098103)
4. Sokolov A, Aranson IS, Kessler JO, Goldstein RE. 2007 Concentration dependence of the collective dynamics of swimming bacteria. *Phys. Rev. Lett.* **98**, 158102. (doi:10.1103/PhysRevLett.98.158102)
5. Sokolov A, Aranson IS. 2012 Physical properties of collective motion in suspensions of bacteria. *Phys. Rev. Lett.* **109**, 248109. (doi:10.1103/PhysRevLett.109.248109)

6. Dunkel J, Heidenreich S, Drescher K, Wensink HH, Goldstein RE. 2013 Fluid dynamics of bacterial turbulence. *Phys. Rev. Lett.* **110**, 228102. (doi:10.1103/PhysRevLett.110.228102)
7. Ryan SD, Haines BM, Berlyand L, Ziebert F, Aranson IS. 2011 Viscosity of bacterial suspensions: hydrodynamic interactions and self-induced noise. *Phys. Rev. E* **83**, 050904. (doi:10.1103/PhysRevE.83.050904)
8. Saintillan D, Shelley M. 2008 Instabilities and pattern formation in active particle suspensions: kinetic theory and continuum simulations. *Phys. Rev. Lett.* **100**, 178103. (doi:10.1103/PhysRevLett.100.178103)
9. Aranson IS, Sokolov A, Kessler JO, Goldstein RE. 2007 Model for dynamical coherence in thin films of self-propelled microorganisms. *Phys. Rev. E* **75**, 040901. (doi:10.1103/PhysRevE.75.040901)
10. Wensink HH, Dunkel J, Heidenreich S, Drescher K, Goldstein RE, Lwen H, Yeomans JM. 2012 Meso-scale turbulence in living fluids. *Proc. Natl Acad. Sci. USA* **109**, 14 308–14 313. (doi:10.1073/pnas.1202032109)
11. Ryan SD, Sokolov A, Berlyand L, Aranson IS. 2013 Correlation properties of collective motion in bacterial suspensions. *New J. Phys.* **15**, 105021. (doi:10.1088/1367-2630/15/10/105021)
12. Cisneros LH, Kessler JO, Ganguly S, Goldstein RE. 2011 Dynamics of swimming bacteria: transition to directional order at high concentration. *Phys. Rev. E* **83**, 061907. (doi:10.1103/PhysRevE.83.061907)
13. Adler J. 1966 Chemotaxis in bacteria. *Science* **153**, **708–716**, 1966. (doi:10.1126/science.153.3737.708)
14. Vogel R, Stark H. 2012 Motor-driven bacterial flagella and buckling instabilities. *Eur. Phys. J. E* **35**, 1–15. (doi:10.1140/epje/i2012-12015-0)
15. Vogel R, Stark H. 2013 Rotation-induced polymorphic transitions in bacterial flagella. *Phys. Rev. Lett.* **110**, 158104. (doi:10.1103/PhysRevLett.110.158104)
16. Son K, Guasto JS, Stocker R. 2013 Bacteria can exploit a flagellar buckling instability to change direction. *Nat. Phys.* **9**, 494–498. (doi:10.1038/nphys2676)
17. Bretherton FP, Rotshchild L. 1961 Rheotaxis of spermatozoa. *Proc. R. Soc. Lond. B* **153**, 490–502. (doi:10.1098/rspb.1961.0014)
18. Miki K, Clapham DE. 2013 Rheotaxis guides mammalian sperm. *Curr. Biol.* **23**, 443–452. (doi:10.1016/j.cub.2013.02.007)
19. Kantsler V, Dunkel J, Blayney M, Goldstein RE. 2014 Rheotaxis facilitates upstream navigation of mammalian sperm cells. *eLife* **3**, e02403.
20. Denissenko P, Kantsler V, Smith DJ, Kirkman-Brown J. 2012 Human spermatozoa migration in microchannels reveals boundary-following navigation. *Proc. Natl Acad. Sci. USA* **109**, 8007–8010. (doi:10.1073/pnas.1202934109)
21. Kantsler V, Dunkel J, Polin M, Goldstein RE. 2012 Ciliary contact interactions dominate surface scattering of swimming eukaryotes. *Proc. Natl Acad. Sci. USA* **110**, 1187–1192. (doi:10.1073/pnas.1210548110)
22. Zöttl A, Stark H. 2012 Nonlinear dynamics of a microswimmer in Poiseuille flow. *Phys. Rev. Lett.* **108**, 21804. (doi:10.1103/PhysRevLett.108.218104)
23. Zöttl A, Stark H. 2012 Periodic and quasiperiodic motion of an elongated microswimmer in Poiseuille flow. *Eur. Phys. J. E* **36**, 1–10.
24. Chilukuri S, Collins CH, Underhill PT. 2014 Impact of external flow on the dynamics of swimming microorganisms near surfaces. *J. Phys. Condensed Matter* **26**, 115101. (doi:10.1088/0953-8984/26/11/115101)
25. Berke AP, Turner L, Berg HC, Lauga E. 2008 Hydrodynamic attraction of swimming microorganisms by surfaces. *Phys. Rev. Lett.* **101**, 038102. (doi:10.1103/PhysRevLett.101.038102)
26. Drescher K, Dunkel J, Cisneros LH, Ganguly S, Goldstein RE. 2011 Fluid dynamics and noise in bacterial cell–cell and cell surface scattering. *Proc. Natl Acad. Sci. USA* **108**, 10 940–10 945. (doi:10.1073/pnas.1019079108)
27. Rusconi R, Guasto JS, Stocker R. 2014 Bacterial transport suppressed by fluid shear. *Nat. Phys.* **10**, 212–217. (doi:10.1038/nphys2883)
28. Taylor GI. 1952 The action of waving cylindrical tails in propelling microscopic organisms. *Proc. R. Soc. Lond. A* **221**, A211–A225. (doi:10.1098/rspa.1952.0035)
29. Purcell EM. 1997 The efficiency of propulsion by a rotating flagellum. *Proc. Natl Acad. Sci. USA* **94**, 11 307–11 311. (doi:10.1073/pnas.94.21.11307)
30. Jung S, Mareck K, Fauci L, Shelley JM. 2007 Rotational dynamics of a superhelix towed in a Stokes fluid. *Phys. Fluids* **19**, 103–105. (doi:10.1063/1.2800287)
31. Marcos H, Fu C, Powers TR, Stocker R. 2012 Bacterial rheotaxis. *Proc. Natl Acad. Sci. USA* **109**, 4780–4785. (doi:10.1073/pnas.1120955109)
32. Kessler JO. 1985 Hydrodynamic focusing of motile algal cell. *Nature* **313**, 218–220. (doi:10.1038/313218a0)
33. Karp-Boss L, Boss LE, Jumars PA. 2000 Motion of dinoflagellates in a simple shear flow. *Limnol. Oceanogr.* **45**, 1596–1602. (doi:10.4319/lo.2000.45.7.1594)
34. Jeffery GB. 1922 The motion of ellipsoidal particles in a viscous fluid. *Proc. R. Soc. Lond. A* **179**, 102–161. (doi:10.1098/rspa.1922.0078)
35. Sokolov A, Aranson IS. 2009 Reduction of viscosity in suspension of swimming bacteria. *Phys. Rev. Lett.* **103**, 148101. (doi:10.1103/PhysRevLett.103.148101)
36. Gachelin J, Miño G, Berthet H, Lindner A, Rousselet A, Clément E. 2013 Non-Newtonian viscosity of *Escherichia coli* suspensions. *Phys. Rev. Lett.* **110**, 268103. (doi:10.1103/PhysRevLett.110.268103)
37. Haines BM, Sokolov A, Aranson IS, Berlyand L, Karpeev DA. 2009 Three-dimensional model for the effective viscosity of bacterial suspensions. *Phys. Rev. E* **80**, 041922. (doi:10.1103/PhysRevE.80.041922)
38. DiLuzio WR, Turner L, Mayer M, Garstecki P, Weibel DB, Berg HC, Whitesides GW. 2005 *Escherichia coli* swim on the right-hand side. *Nature* **435**, 1271–1274. (doi:10.1038/nature03660)
39. Batchelor GK. 1970 Slender-body theory for particles of arbitrary cross-section in Stokes flow. *J. Fluid Mech.* **44**, 419–440. (doi:10.1017/S002211207000191X)
40. Roper M, Dreyfus R, Baudry J, Fermigie M, Bibette J, Stone HA. 2006 On the dynamics of magnetically driven elastic filaments. *J. Fluid Mech.* **554**, 167–190. (doi:10.1017/S0022112006009049)
41. Segré G, Silverberg A. 1962 Behaviour of macroscopic rigid spheres in Poiseuille flow. *J. Fluid Mech.* **14**, 136–157. (doi:10.1017/S0022112062001111)
42. Berg HC. 2004 E. coli *in motion*. Berlin, Germany: Springer.
43. Saffman PG. 1965 The lift on a small sphere in a slow shear flowing. *J. Fluid Mech.* **22**, 385–400. (doi:10.1017/S0022112065000824)

Glossary

α	drag anisotropy factor
β	Bretherton constant of the ellipsoidal body
γ	shear rate
d	thickness of the body
η_0	viscosity of the surrounding fluid
F_P	propulsion force density
K_b	bending stiffness
k_r	non-dimensional parameter
Λ	internal stress of the flagellum (tangential part)
λ_r	parameter of the Poisson process
L	length of the flagellum
l	length of the body
N	internal stress of the flagellum (normal part)
p	pressure gradient of the Poiseuille flow
s	current coordinate on the flagellum
t	time
θ_0	body angle (swimmer orientation)
θ	angle of the flagellum
$(\tau, \mathbf{n}, \mathbf{b})$	Frenet system
u	fluid velocity
(v_τ, v_n)	flagellum velocity in Frenet coordinates
$(v_{\tau,0}, v_{n,0})$	body velocity in Frenet coordinates
w	radius of the channel
(x^h, y^h)	coordinate of the body centre
ζ_f	friction coefficient for the flagellum
ζ_h	friction coefficient for the head